

## NEW CONSTRAINTS ON PROTOSTELLAR JET COLLIMATION FROM HIGH-DENSITY GAS UV TRACERS<sup>1</sup>

ANA I. GÓMEZ DE CASTRO

Instituto de Astronomía y Geodesia, Facultad de CC. Matemáticas, Universidad Complutense de Madrid, 28040-Madrid, Spain;  
 aig@eucmos.sim.ucm.es

AND

EVA VERDUGO

ISO Data Centre, VILSPA, P.O. Box 50727, 28080 Madrid, Spain; everdugo@iso.vilspa.esa.es

Received 1999 December 14; accepted 2000 October 9

### ABSTRACT

The analysis of high-resolution profiles of the semiforbidden UV lines of C III]<sub>1908</sub> and Si III]<sub>1892</sub> in the spectra of T Tauri stars (TTs) shows the following: (1) There is C III]<sub>1908</sub> and Si III]<sub>1892</sub> emission at velocities that are similar to those observed in the optical forbidden lines formed in the TTs jets. The luminosity of the UV lines is comparable to that of the optical lines. (2) The comparison between the optical and UV light curves indicates that the C III]<sub>1908</sub> and Si III]<sub>1892</sub> emission of RY Tau is not associated with accretion shocks, but it is produced farther than  $2 R_*$  from the star. (3) The profiles of the UV semiforbidden lines are significantly broader than those of the optical forbidden lines. These profiles cannot be produced in a narrow collimated beam, and they are most likely produced in a bow-shaped shock wave formed at the base of the optical jet, where the hot gas emits in a broad range of projected radial velocities. (4) The atmosphere of RU Lup contributes significantly to the Si III]<sub>1892</sub> emission. (5) A puzzling narrow feature is observed close to the C III]<sub>1908</sub> line. The feature is blueshifted by  $-260 \text{ km s}^{-1}$ , which corresponds to the wind terminal velocity measured in the P Cygni profile of the Mg II (UV1) lines. Moreover, constraints are derived on the characteristics of the C III]<sub>1908</sub> and Si III]<sub>1892</sub> emitting region in RY Tau. It is shown that  $4.7 \leq \log T_e \leq 5.0$  and  $10^9 \text{ cm}^{-3} \leq N_e \leq 10^{11} \text{ cm}^{-3}$  provided that the emission is produced in a collisional plasma and that the 1665 Å feature observed in low-dispersion *International Ultraviolet Explorer* (IUE) spectra is confirmed to be O III]<sub>1665</sub> emission produced in the wind. These very high densities are difficult to generate in the shocks produced by the magnetic pinching of centrifugally driven magnetized disk winds. The data also suggest that the shocked layer has a radius of some few stellar radii and it is closer than  $\sim 38 R_*$  to the star.

*Subject headings:* stars: individual (RU Lupi, RY Tauri) — stars: mass loss — stars: pre-main-sequence stars: variables: other

### 1. INTRODUCTION

Outflow is ubiquitous during star formation. Some basic models have been proposed to explain how this outflow may be driven (see Koenigl & Pudritz 2000 and Shu et al. 2000 for recent reviews). In these models the outflow is assumed to be powered by the gravitational energy released during the accretion process, and the magnetic field is often hypothesized as the physical stress that efficiently channels the gravitational energy into the mechanical outflow energy. Determining the physical mechanism that connects accretion to outflow is one of the key issues in star formation since this regulates the accretion rate and the evolution during star formation. Moreover, it seems likely that the same physics applies to other astrophysical systems, such as quasistellar objects, active galactic nuclei, or microquasars.

To obtain information about the physics of jet formation it is necessary to go below scales of  $\sim 1000 \text{ AU}$ . Ground-based and *Hubble Space Telescope* (HST) observations have allowed us to measure the jet diameter within  $140 \text{ AU}$  ( $1''$

for the nearest star-forming regions) and derive constraints on jet collimation (see Eisloffel et al. 2000 for a recent review). In particular, Hirth, Munth, & Solf (1997) have shown from various long-slit spectroscopic studies in the nearby Taurus-Auriga cloud that the jet emission originates at different distances from the source for different spectral tracers. The emission from the [O I]<sub>6300</sub> line peaks at around  $0.2$  (28 AU) from the source, while the emission from the [S II]<sub>6731</sub> and [N II]<sub>6584</sub> lines are factors of 3 and 3.5 further away, respectively. As the [O I]<sub>6300</sub> line has a critical density around 100 times higher than the [S II]<sub>6731</sub> line, these observations suggest that the jet streamlines diverge with the distance from the source, giving rise to a drop in density. Unfortunately, the observational information about how outflow is initiated is contained within a region of angular size smaller than  $0.1$  (for the nearest star-forming regions) which is not accessible to direct imaging. If the density of the jet increases toward the source, the electron density at the base of the jet could be even higher than the  $10^6 \text{ cm}^{-3}$  traced by the [O I]<sub>6300</sub> optical line. The UV semiforbidden lines are optimal tracers at these very high densities.

The C III]<sub>1908</sub> ( $2s^2S_1-2s2p^3P_1$ ) and Si III]<sub>1892</sub> ( $3s^2S_1-3s3p^3P_1$ ) UV intercombination lines are strong in the spectrum of the TTs. A quick look at the *International Ultraviolet Explorer* (IUE) Final Archive shows that the

<sup>1</sup> Based on observations made with the *International Ultraviolet Explorer* (IUE) and with the NASA/ESA *Hubble Space Telescope* obtained from the HST data archive at the Space Science Institute, which is operated by the Association of Universities for Research in Astronomy Inc., under NASA contract NAS 5-26555.

Si III]<sub>1892</sub> line is detected in 21 stars and the C III]<sub>1908</sub> in 19 stars, from a grand total of 36. Their detection was first reported for T Tau by Jordan, Ferraz, & Brown (1982); subsequent studies used these lines to derive the emission measure and model the structure of the atmosphere of the TTSs (see e.g. Gómez de Castro 1997 for a recent review). The ratio  $I(\text{Si III}]_{1892})/I(\text{C III}]_{1908})$  is density sensitive, and it is often used to estimate electron densities in late-type stellar atmospheres within the range  $10^8 \leq N_e \leq 10^{13} \text{ cm}^{-3}$  (see Brown, Ferraz, & Jordan 1984 for its application to T Tau). Recently, it has been shown that these lines could also be formed in accretion shocks (shocks where the kinetic energy from the material falling onto the stellar surface is released); the C III]<sub>1908</sub> and Si III]<sub>1892</sub> lines are expected, then, to be formed before the shock front, where the infalling gas is ionized by the X-ray radiation produced in the hot ( $T \sim 10^6 \text{ K}$ ) postshock region (Lamzin 1998; Gómez de Castro & Lamzin 1999). Particle density in the accretion column is typically between  $10^{10}$  and  $10^{13} \text{ cm}^{-3}$ . Moreover, the C III]<sub>1908</sub> and Si III]<sub>1892</sub> lines could also be excited in dense shocks at the base of the jet, where the material from a dense wind is collimated into a narrow beam of gas. In summary, these lines are an extraordinary diagnosis tool to study the major physical processes in the hot dense circumstellar environment around the TTSs.

An additional advantage of these tracers is that they are accompanied by a nearby forbidden component and the ratios between the forbidden and the intercombination components of the C III]<sub>1907, 1909</sub> and Si III]<sub>1883, 1892</sub> multiplets are sensitive to electron densities in the range  $N_e \simeq 10^3\text{--}10^6 \text{ cm}^{-3}$  (Keenan, Feibelman, & Berrington 1992). Therefore, a high-resolution UV spectrum in the 1880–1910 Å spectral range provides direct diagnosis on electron densities over nearly 10 orders of magnitude! This is an ideal tool for the study of the TTSs environment, where many physical components are expected to be present and cannot be resolved spatially.

In this work, we present the results of a search for these lines in high-resolution UV spectra obtained either with the *IUE* or with the *HST*. These lines have been detected in three pre-main-sequence stars: AB Dor, RU Lup, and RY Tau. The line emission from AB Dor seems to be caused in infalling gas (Gómez de Castro 2001), while in RU Lup and

RY Tau we have found evidence of the line being produced in a very dense wind at the base of the jet traced by the optical forbidden lines. In § 2 the archive data are shown. In § 3 the data on RY Tau are analyzed and it is shown that the lines are most probably emitted in a bow-shaped structure located at the base of the jet. The RU Lup data are analyzed in § 4, where it is shown that the line emission is produced partly in the stellar atmosphere, partly in the wind. In § 5 we discuss the relevance of these results on jet collimation and a brief summary of the results is presented in § 6.

## 2. ARCHIVE DATA

We have searched the *IUE* and *HST* archive for high-resolution profiles of the C III]<sub>1908</sub> and Si III]<sub>1892</sub> semi-forbidden lines in the TTSs. A summary with the available information is provided in Table 1.

### 2.1. The *IUE* Data

The *IUE* high-dispersion ( $R \sim 10,000$ ) data were obtained with an echelle spectrograph and a SEC integrating video camera as detector. The Si III]<sub>1892</sub> line is well centered in order 73, and the C III]<sub>1908</sub> line is close to the blue edge of the order 72 (1905.3–1926.6 Å); these two lines are displayed in Figure 1 for the TTSs observed with the *IUE*. Notice that the Si III]<sub>1892</sub> line is clearly detected only in RU Lup. Marginal detection of the Si III]<sub>1892</sub> feature can be claimed for T Tau (SWP15475) and RW Aur (SWP49878). The C III]<sub>1908</sub> line is detected only in RU Lup (and only in the spectrum SWP19736), suggesting that the line is variable. These two lines have been detected in the *IUE* low-dispersion spectra of T Tau, DR Tau, SU Aur, RW Aur, and RU Lup (see Gómez de Castro & Franqueira 1997, hereafter GF).

The data used in this work have been processed with the *IUE* Newly Extracted Spectra (INES) system, which introduces some improvements with respect to the system used for the *IUE* Final Archive (NEWSIPS; Rodriguez et al. 1999). The internal accuracy on the wavelength determination provided by the *IUE* high-resolution spectra processed with NEWSIPS is  $4.2(\pm 1.5) \text{ km s}^{-1}$ ; however, the comparison between the short wavelength (SWP) and the long wavelength (LWR and LWP) cameras indicates that it

TABLE 1  
LOG OF DATA

CHARACTERISTICS OF THE OBSERVATIONS							
HBC	OBJECT	INSTRUMENT	Date	$T_{\text{exp}}$ (s)	Observation ID	Si III]	C III]
34 .....	RY Tau	<i>HST</i> + GHRS (Grid: G200M)	31/DEC/93	01496	Z1E70108T	Y	Y
35 .....	T Tau	<i>IUE</i> (HRes)	04/JAN/81	24420	SWP10955		
		<i>IUE</i> (HRes)	11/NOV/81	53400	SWP15475	Y?	
		<i>IUE</i> (HRes)	17/OCT/85	68700	SWP26948		
74 .....	DR Tau	<i>IUE</i> (HRes)	12/JAN/89	50100	SWP35327		
79 .....	SU Aur	<i>IUE</i> (HRes)	03/FEB/95	45900	SWP53816		
80 .....	RW Aur	<i>IUE</i> (HRes)	23/JAN/94	39000	SWP49878	Y?	
251 .....	RU Lup	<i>IUE</i> (HRes)	13/SEP/81	21660	SWP14980	Y	
		<i>IUE</i> (HRes)	16/APR/83	45300	SWP19736	Y	Y
		<i>HST</i> + GHRS (Grid: G200M)	24/AUG/92	01496	Z10T0109M	Y	Y
568 .....	TW Hya	<i>IUE</i> (HRes)	08/JAN/83	24240	SWP18967		
		<i>IUE</i> (HRes)	15/JUL/84	48600	SWP23467		
		<i>IUE</i> (HRes)	17/JUL/84	02400	SWP23472		

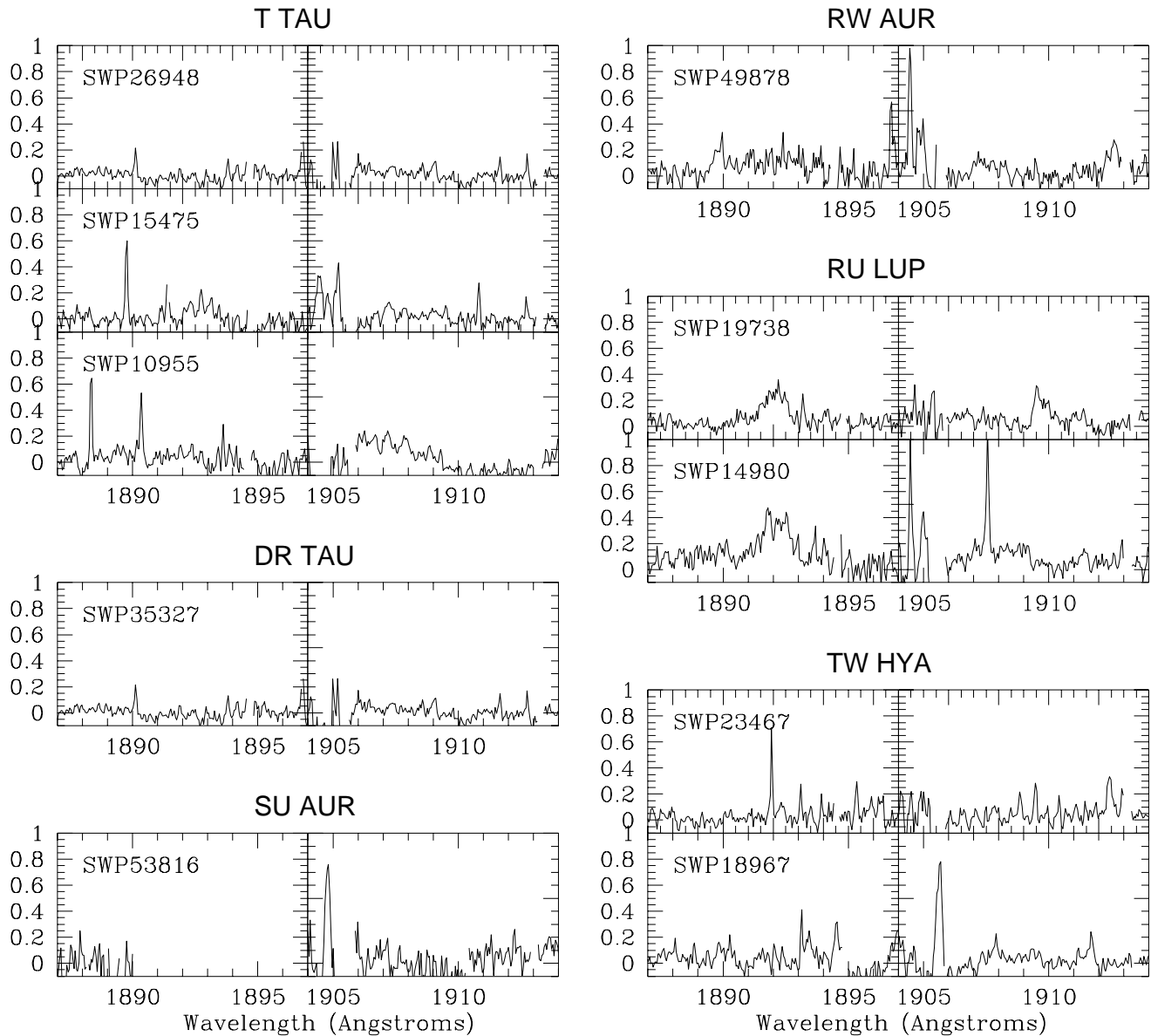


FIG. 1.—Profiles of the  $\text{Si III}]_{1892}$  and  $\text{C III}]_{1908}$  lines of the TTSs as obtained with the *IUE* in high-resolution mode. The SWP23472 spectrum of TW Hya is not represented because it is very noisy. The flux (y-axis) is given in units of  $10^{-12} \text{ ergs s}^{-1} \text{ cm}^{-2} \text{ \AA}^{-1}$ .

is necessary to add a  $+17.7 (\pm 4.4) \text{ km s}^{-1}$  velocity correction to the large-aperture SWP data for self-consistency of the *IUE* final data (González-Riestra et al. 2000). This correction is directly applied to the INES data.

## 2.2. The HST Data

The *HST*-GHRS medium resolution ( $R \sim 25,000$ ) data were obtained with the first-order grating G200M and the photon-counting Digicon detector D2. The  $\text{Si III}]_{1892}$  and

$\text{C III}]_{1908}$  lines were well centered in the detector, which typically covered the 1880–1920 Å spectral range.

The *HST* + GHRS have been processed using the IRAF/STSDAS package. The groups within a given data set have been aligned using the wavelength information provided with the calibrated *HST* data file and then co-added to produce the line profiles represented in Figure 2. The  $\text{Si III}]_{1892}$  and  $\text{C III}]_{1908}$  lines are clearly detected in the RY Tau and RU Lup spectra.

TABLE 2  
FUNDAMENTAL PARAMETERS OF RY TAU AND RU LUP

Object	Spectral Type	$\log T_{\text{eff}}$	$\log (L/L_{\odot})$	$R/R_{\odot}$	$A_V$	[O I] $\lambda 6300^a$	[S II] $\lambda 6731^a$	Reference
RY Tau .....	K1	3.706	0.54	2.4	0.55	$1.29 \times 10^{-13}$	$1.96 \times 10^{-14}$	1
RU Lup .....	K7-M0	3.591	0.33	1.6	1.28			2, 3

<sup>a</sup> Dereddened flux in the lines in  $\text{ergs cm}^{-2} \text{ s}^{-1}$ .

REFERENCES.—(1) Hartigan, Edwards & Ghandour 1995; (2) Hughes et al. 1994; (3) Lamzin et al. 1996.

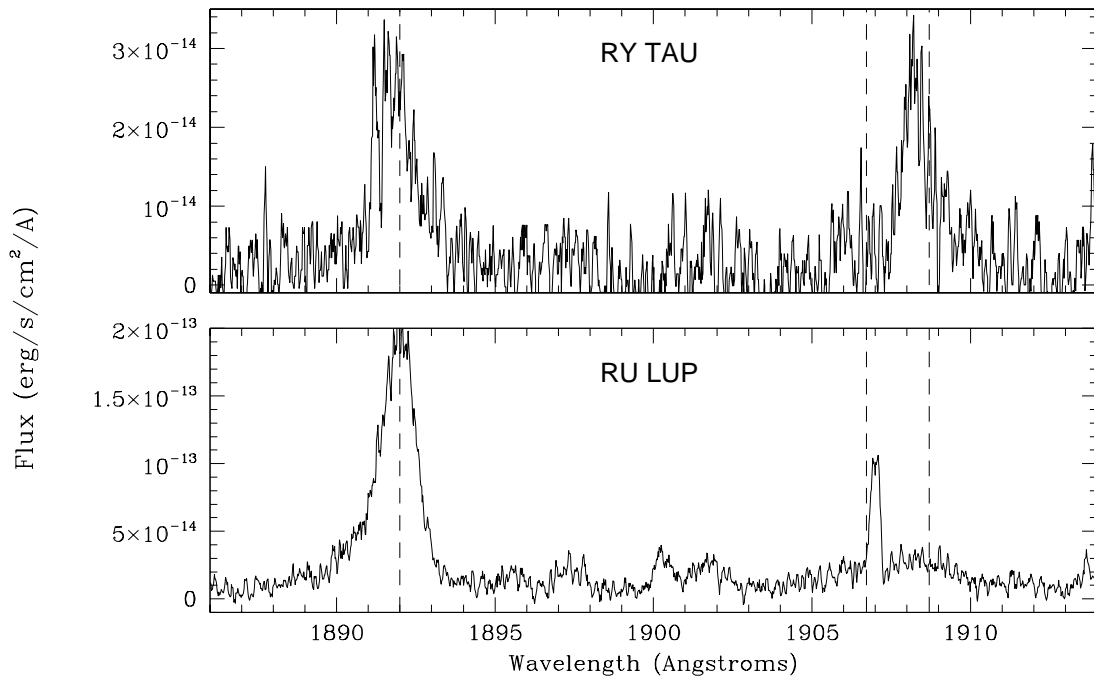


FIG. 2.—Profiles of the  $\text{Si III}]_{1892}$  and  $\text{C III}]_{1908}$  lines of the TTSs as obtained with the *HST* and the GHRs

Dead (or problematic) diodes during the observations that are close to the  $\text{Si III}]_{1892}$  and  $\text{C III}]_{1908}$  lines are at wavelengths 1888, 1891.4, 1901.5, and 1907 Å for RY Tau and at 1888, 1891.4, and 1901.5 Å for RU Lup. In all cases, it was possible to determine the flux uncertainty during the calibration, and this is provided in the propagated error file.

The GHRs data were obtained with the Large Science Aperture (LSA) and in this case, the major sources of inaccuracies in the wavelength calibration are the centering of the target in the aperture and the lack of an accurate incidence angle correction for the LSA; these errors can account for as much as 1.5 diodes (Lindler 1993), which is equivalent to 0.12 Å (20 km s<sup>-1</sup>) in our data.

The main characteristics of RY Tau and RU Lup are summarized in Table 2.

### 3. RY TAU

The  $\text{C III}]_{1908}$  and  $\text{Si III}]_{1892}$  lines profiles are similar: they are asymmetric, with the maximum blueshifted to radial velocity  $\sim -80$  km s<sup>-1</sup> and an extended red wing which reaches  $V_r \sim +200$  km s<sup>-1</sup> (see Fig. 3). The  $\text{Si III}]_{1892}$  line is broader than the  $\text{C III}]_{1908}$  ( $\text{FWHM}(\text{Si III}]_{1892}) = 230$  km s<sup>-1</sup> and  $\text{FWHM}(\text{C III}]_{1908}) = 150$  km s<sup>-1</sup>); also the red wing is more apparent in the  $\text{Si III}]_{1892}$  line. The slight difference between the two profiles is within the error bars of the GHRs measurements; there is also a bad diode (no. 144) at a wavelength of  $\sim 1891.6$  Å very close to the core of the  $\text{Si III}]_{1892}$  line, which could contribute to this difference.

The asymmetric blueshifted  $\text{C III}]_{1908}$  and  $\text{Si III}]_{1892}$  profiles indicate that these lines are most likely formed in the wind. In fact, the blueshift of the high-velocity component of the optical forbidden line of  $[\text{O I}]_{6300}$  at 6300 Å is similar to the one detected in the  $\text{C III}]_{1908}$  and  $\text{Si III}]_{1892}$  lines; the  $[\text{O I}]_{6300}$  emission is centered at  $-79$  km s<sup>-1</sup> (Hamann 1994; Hartigan, Edwards, & Ghandour 1995; Hirth et al. 1997; Edwards et al. 1987). However, the  $[\text{O I}]_{6300}$  line is significantly narrower ( $\text{FWHM} = 70$  km s<sup>-1</sup>) than the UV

semiforbidden lines. High-resolution long-slit spectra show no offset between the high-velocity  $[\text{O I}]_{6300}$  emission and the stellar position, pointing out that this line forms within  $\sim 42$  AU of the star.

Wind emission has also been detected in the optical forbidden lines of  $[\text{Fe II}]$  at 7155 Å and of  $[\text{S II}]$  at 6731 Å. The  $[\text{Fe II}]_{7155}$  line has an asymmetric profile similar to the one observed in the  $\text{C III}]_{1908}$  and  $\text{Si III}]_{1892}$  lines although no

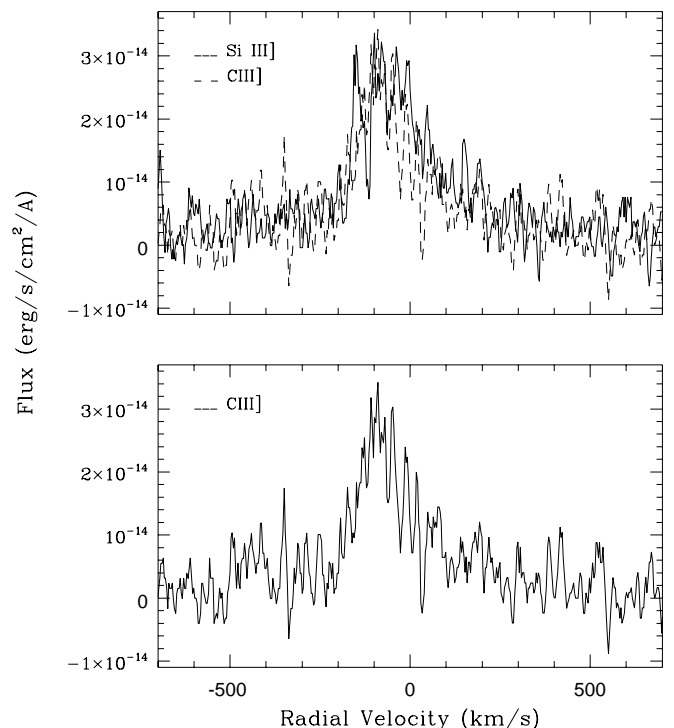


FIG. 3.—RY Tau  $\text{Si III}]_{1892}$  and  $\text{C III}]_{1908}$  profiles plotted in velocity space. The profiles have been smoothed with a boxcar of width 1.5 diodes.

red-extension is apparent as in the UV lines. The  $[\text{S II}]_{6731}$  line is very weak and the high-velocity component detection seems to be marginal (compare Hartigan et al. 1995 and Hirth et al. 1997 with Hamann 1994). No detection of  $[\text{O I}]$  emission at  $5577 \text{ \AA}$  and  $[\text{S II}]$  at  $6716 \text{ \AA}$  has been reported.

In summary, the profiles of the UV semiforbidden lines are significantly broader than those of the optical forbidden lines. This broad UV profile cannot be produced in a narrow collimated beam of gas. The most likely source is emission from a bow shock (a series of oblique plane shocks having as a consequence a range of velocities in the shock wave). Therefore, the UV lines are most probably formed in a bow-shaped structure which is within 42 AU of the star; the unresolved “black box.”

### 3.1. Physical Properties of the Line Formation Region

Neither the  $[\text{C III}]_{1907}$  nor the  $[\text{Si III}]_{1883}$  forbidden lines have been detected in the *HST* spectrum; this imposes a lower limit to the electron density of  $N_e \geq 10^5 \text{ cm}^{-3}$  since  $R_1 = [\text{C III}]_{1907}/[\text{C III}]_{1909} \leq 0.25$  (Keenan et al. 1992). At this high electron density the  $[\text{S II}]$  doublet is collisionally depopulated, which is also consistent with the very low strength of  $[\text{S II}]_{6731}$  and the nondetection of the  $[\text{S II}]_{6716}$  line.

The  $R_2 = [\text{Si III}]_{1892}/[\text{C III}]_{1908}$  line ratio is electron-density sensitive at higher densities ( $N_e \approx 10^9 \text{ cm}^{-3}$ ). The integrated fluxes of the  $[\text{Si III}]_{1892}$  and  $[\text{C III}]_{1908}$  lines are  $F([\text{Si III}]_{1892}) = (3.4 \pm 1) \times 10^{-14} \text{ ergs s}^{-1} \text{ cm}^{-2}$  and  $F([\text{C III}]_{1908}) = (3.2 \pm 0.8) \times 10^{-14} \text{ ergs s}^{-1} \text{ cm}^{-2}$ , respectively, so  $R_2 = 1.1 \pm 0.4$  for RY Tau.

To derive a constraint on the density from this line ratio it is necessary to make assumptions on the ionization mechanism and the lines excitation process. As a first approach, let us assume that the semiforbidden lines (SL) emission is produced in a collisionally dominated plasma. The effect of photoionization by coronal X-rays is expected to be significant only close to the star because the geometrical dilution of the radiation field and the high density of the SL formation region ( $N \geq 10^6 \text{ cm}^{-3}$ ). Photoionization could be important if the SL formed in the photoionized precursor of low-density strong shocks ( $V \geq 200 \text{ km s}^{-1}$ ); a discussion on this issue is deferred to § 5.

The value of  $R_2$  obtained for RY Tau is compared in Figure 4 with the theoretical predictions by Keenan, Dufton, & Kingston (1987), where this ratio is tabulated for three electron temperatures,  $\log T_e = 4.5, 4.7$ , and  $4.9$ , which cover the range over which the  $[\text{Si III}]_{1892}$  and  $[\text{C III}]_{1908}$  lines are formed in collisional ionization equilibrium. A solar silicon-to-carbon abundance ratio of  $9.55 \times 10^{-2}$  is assumed. The line ratio is sensitive to the temperature mainly through the ionization fraction, which varies significantly in this narrow range. If the ionization fraction is assumed to be equal to 1,  $R_2$  varies only by a 20% between  $\log T_e = 4.5$  and  $4.9$  at low densities and by a 4% in the high-density limit. To derive the  $R_2$  ratios plotted in Figure 4, we have used the ionization fractions from the ionization balance calculations by Arnaud & Rothenflug (1985), in which only collisional processes are included and the low-density case (Jordan 1969) is assumed. The ionization fraction of C III varies from 0.1 at  $\log T_e = 4.5$  to 0.8 at  $\log T_e = 4.9$  and decreases to 0.4 at  $\log T_e = 5$ . The ionization fraction of Si III is maximum at  $\log T_e = 4.5$  with a value of 0.9 and decreases with the temperature to reach 0.15 at  $\log T_e = 4.9$  and 0.02 at  $\log T_e = 5$ . This implies that

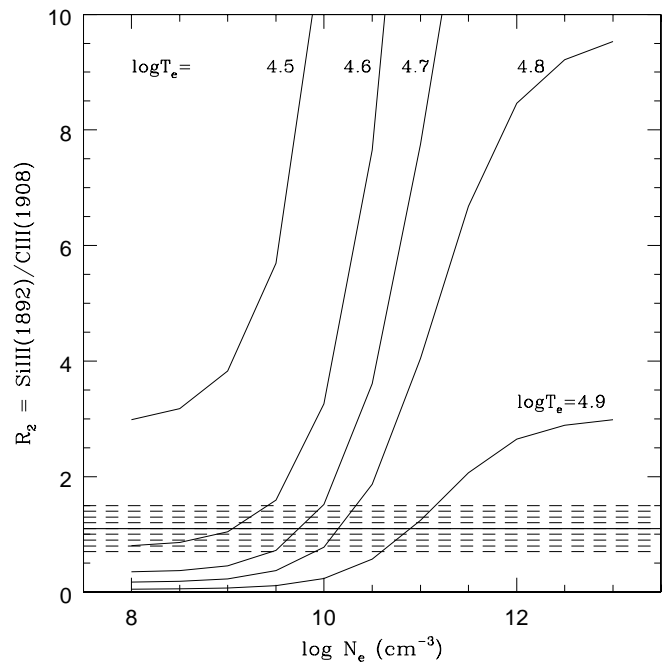


FIG. 4.— $R_2$  as a function of  $\log N_e$  according to Keenan et al. (1987) for  $\log T_e = 4.5, 4.6, 4.7, 4.8$  and  $4.9$  (see text). The range of  $R_2 = 1.1 \pm 0.4$  is represented by a dashed line. The value  $R_2 = 1.1$  is marked with a thick line.

$R_2$  is significantly larger than 1.1 for temperatures below  $\log T_e = 4.5$ , even for densities as small as  $10^8 \text{ cm}^{-3}$ , and significantly smaller than 1.1 for temperatures over  $\log T_e = 5.0$ , even for densities as high as  $10^{13} \text{ cm}^{-3}$ . In this sense,  $R_2$  can be considered as a temperature indicator that points out that the temperature of the emitting gas is somewhat in between  $\log T_e = 4.6$  and 5 (see Fig. 4). The  $[\text{O III}]_{1665}$  intercombination line has been apparently detected in the *IUE* low-dispersion spectra of RY Tau (Gómez de Castro & Lamzin 1999). If the line detection and its association with the jet were confirmed by high-resolution spectra, this would indicate that the temperature of the emitting plasma is  $\log T_e > 4.7$ , and hence the density of the gas would be in the range  $3 \times 10^9 \leq N_e \leq 10^{11} \text{ cm}^{-3}$ .

### 3.2. SL Variability

The SL are variable and, in principle, the  $R_2$  ratio could also be it. The low-dispersion observations available in the *IUE* Final Archive allows checking further this possibility. There are 14 observations available that were obtained between 1979 and 1989 (see GF for further information). The SL fluxes varied by as much as a factor of 3 during this period, and variations by a factor of  $\approx 2$  in line flux are detected between observations taken just 2 days apart. As shown in Figure 5 the  $R_2$  ratio varied within a range between 0.8 and 1.8 during the *IUE* lifetime, the average value being  $1.35 \pm 0.3$ . This range corresponds quite well with the error band plotted in Figure 4. The most significant variations are found between the observations obtained in 1986 and the rest. There also seem to be significant variations between observations obtained just few days apart as those corresponding to the monitoring campaign run in 1989 January (see GF for more details); in this case the ratio increased by 40% (from 1.25 to 1.75) in just 2 days. Also,

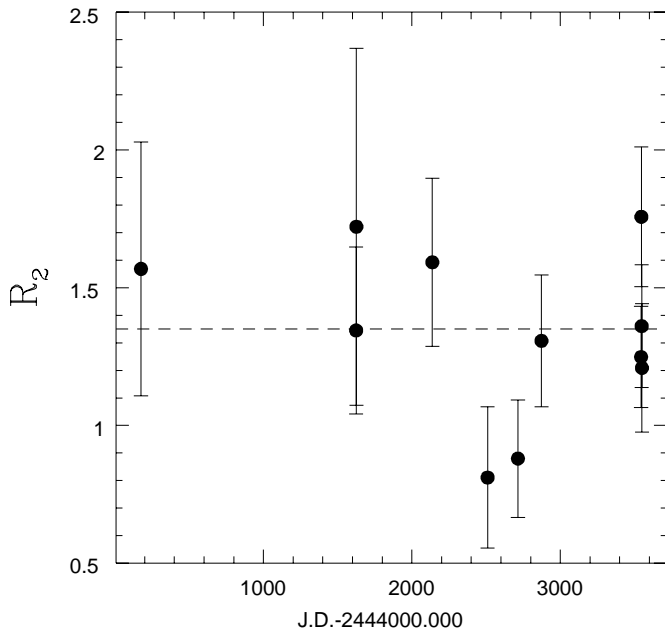


FIG. 5.—Variation of RY Tau SL ratio between 1979 and 1989, based on *IUE* low-dispersion data. The dashed line represents the  $R_2$  value (1.35) determined from the high-resolution *HST* spectra.

significant variations (by a factor of  $\sim 2$ ) have been detected between observations taken just 18 hr apart on 1983 October 18. There could be three major causes of this very rapid variation:

1. *Eclipses.*— RY Tau has been classified as an UX Ori star (UXor) or pre-main-sequence star that shows aperiodic eclipse-like minima caused by variable obscuration by circumstellar dust (Grinin 1992). In this case, there should be a correlation between the line flux variations and the optical magnitude. It is feasible to study this correlation for the *IUE* data since the visual magnitude of RY Tau was also measured with the Fine Error Sensor (FES) at the beginning of each observation. The FES gives estimates of the visual magnitude with rms errors of 0.08 mag and rms errors associated with the reproducibility even better: just  $\sim 0.04$  mag (Holm & Rice 1981). The FES measurements have been converted into magnitudes using Stickland's (1980) calibration for the 1978–1980 data and Perez's (1991) for the monitoring campaign data. They have been corrected from color effects, the sensitivity degradation of the cameras (Fireman & Imhoff 1989), and the change of the FES reference point after 1990 July in VILSPA. As shown in Figure 6, there is no correlation between the optical magnitude and the lines variation; therefore, whatever is obscuring the star (protoplanet, circumstellar dust or accretion column, or shell) is not obscuring the SL formation region. This, in turn, implies that this region must be further away than  $1\text{--}2 R_*$  and discards its connection with accretion shocks (Lamzin 2000).

2. *Variations of the emissivity.*—As the  $\text{Si III}]_{1892}$  and  $\text{C III}]_{1908}$  lines are optically thin, the reported variations cannot be caused by changes in the viewing angle of the line emission region. In fact, they can be accounted for only by intrinsic variations associated with either the development of internal instabilities in the shocked gas layer or the formation of dust clumps in the outflow (variable extinction). We can rule out this last possibility because the  $R_2$  ratio

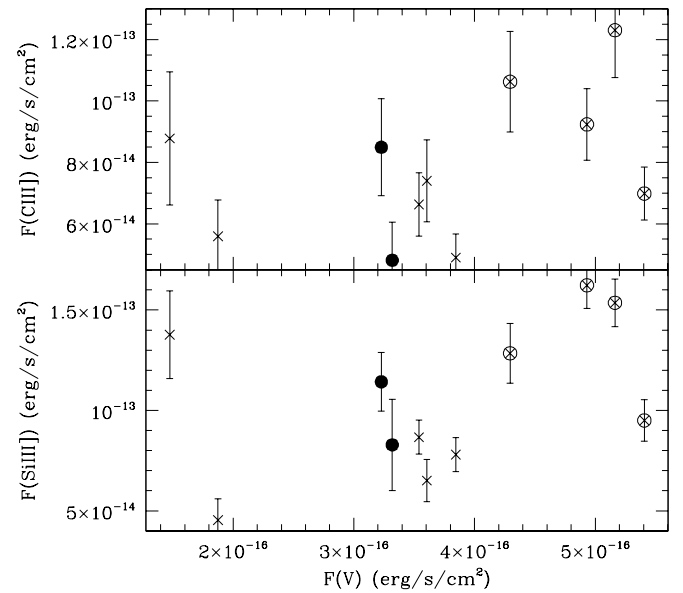


FIG. 6.—Variation of RY Tau SL fluxes with the optical flux derived from  $V$  magnitudes obtained with the *IUE* FES Camera. The observations were obtained with the *IUE* between 1979 and 1989. The data marked with filled and open circles correspond to monitoring campaigns carried out in 1986 and 1989, respectively.

varies during timescales similar to those of the lines fluxes; notice that the  $\text{Si III}]_{1892}$  and  $\text{C III}]_{1908}$  lines have very similar wavelengths and that therefore the  $R_2$  ratio is not sensitive to extinction variations. Moreover, although the detailed physics of the shocked layer is unknown, the high temperature of the gas (typically  $> 30,000$  K) indicates that the characteristic timescale for the development of instabilities ought to be much shorter than a day. In fact, variations caused by these instabilities would be averaged out in the *IUE* data which have typical exposure times of some 6 hr. It would be, anyway, extremely interesting to carry out a short-timescale monitoring of RY Tau to confirm this point.

3. *Variations in the wind properties.*—This seems the most likely cause of variability. In this case, it would be possible to determine the distance between the wind source and the shocked region carrying out a short-timescale monitoring that coordinates observations of spectral tracers at the base of the wind (optical) and in the shocked region (UV). Some further constraints can be derived making assumptions on the wind drive (see § 5).

#### 4. RU LUP

The  $\text{Si III}]_{1892}$  and  $\text{C III}]_{1908}$  line profiles of RU Lup are very different.

The  $\text{Si III}]_{1892}$  line is clearly detected both in the *IUE* and in the *HST* observations including the subexposed *IUE* SWP14980 spectra. In all the spectra the line is very strong and seems to be centered at the stellar velocity. The  $\text{Si III}]_{1892}$  line center has been calculated in all three spectra, and the shifts with respect to the rest wavelength have been measured (see Table 3). The *IUE* measurements are self consistent (see § 2.1). The *HST* wavelength scale is blueward shifted by  $\sim 14.3 \text{ km s}^{-1}$  with respect the best *IUE* measurement (16/APR/83). A comparison between the *IUE* and *HST* wavelength calibrations has been carried out for the

TABLE 3

TEST FOR CONSISTENCY OF THE WAVELENGTH SCALES

Observation	$\lambda$ (Si III] <sub>1892</sub> )	$\Delta\lambda$ ( $\lambda_{\text{Si III]]} - \lambda_0$ )	$\Delta V$ (km s <sup>-1</sup> )
<i>IUE</i> (13/SEP/81) .....	1892.10	0.07	11.1
<i>IUE</i> (16/APR/83) .....	1892.06	0.03	4.8
<i>HST</i> (24/AUG/92) .....	1891.97	-0.06	-9.5

velocity standard  $\zeta$  Oph (González-Riestra et al. 2000); as a result it was found that an additive net velocity correction of  $+9.7$  km s<sup>-1</sup> has to be applied to the *IUE* SWP data. If this correction is applied to the RU Lup spectrum, then the velocity shift would rise to 24 km s<sup>-1</sup>, which is also consistent with the uncertainties in the wavelength calibration for HRS spectra acquired with the LSA. Therefore the Si III]<sub>1892</sub> line maximum can be considered to be at rest within the uncertainties of the *IUE* and *HST* wavelength calibrations. The Si III]<sub>1892</sub> line has a blue wing that extends up to radial velocity  $-300$  km s<sup>-1</sup> (see Fig. 7). The Si III]<sub>1892</sub> profile can be fitted by two Gaussians:

1. A low-velocity component with integrated flux equal to  $2.1 \times 10^{-13}$  ergs s<sup>-1</sup>cm<sup>2</sup> and centered at rest (within the wavelength calibration uncertainties). The FWHM of this component is 185 km s<sup>-1</sup>.
2. A high-velocity component with integrated flux equal to  $6.6 \times 10^{-14}$  ergs s<sup>-1</sup>cm<sup>2</sup> centered at  $-142$  km s<sup>-1</sup>. This component is very broad with FWHM = 337 km s<sup>-1</sup>.

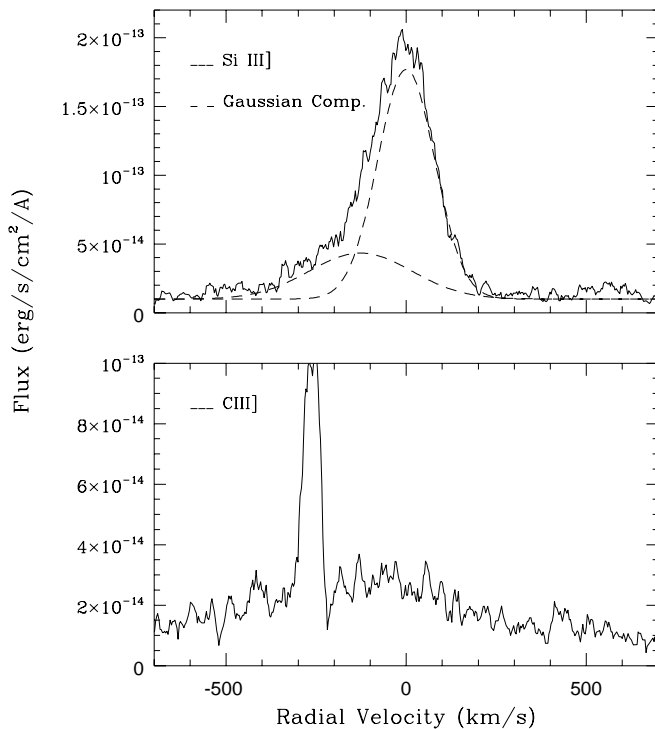


FIG. 7.—Si III]<sub>1892</sub> and C III]<sub>1908</sub> profiles of RU Lup in velocity space; the profiles have been smoothed with a boxcar of width 1.5 diodes. *Top panel*: The Si III]<sub>1892</sub> profile has been fitted by two Gaussians centered at 0 and at  $-142$  km s<sup>-1</sup>, which are represented by a dashed line. *Bottom panel*: The C III]<sub>1908</sub> region is represented; notice the presence of a narrow component with velocity close to the Si III]<sub>1892</sub> profile blue edge.

There is a broad, weak emission feature at  $2\sigma$  level at the location of the C III]<sub>1908</sub> line; the line flux is  $9.0 \times 10^{-14}$  ergs s<sup>-1</sup>cm<sup>2</sup>. This broad component seems to correspond well (in the velocity space) with the blueshifted component of the Si III]<sub>1892</sub> line. As in the case of RY Tau, this indicates that there is Si III]<sub>1892</sub> and C III]<sub>1908</sub> emission produced in the wind. In fact, the velocity of the blueshifted gas is similar to that of the base of the jet traced by the optical forbidden lines (see e.g. Haman 1994); this material is moving at  $\sim -140$  km s<sup>-1</sup>, and it is detected in the [O I]<sub>6300</sub>, the [S II]<sub>4069</sub> and in the [S II]<sub>6731</sub> lines. The UV lines are significantly broader than the optical.

There is a narrow feature at 1907 Å for which we have not found any identification in the Morton tables of UV multiplets. The feature is broader than the instrumental profile (FWHM = 70 km s<sup>-1</sup>) and there is no indication in the propagated error file of any bad diode at this wavelength. This line wavelength is very close to the rest wavelength of the forbidden component of the [C III] multiplet. However, as shown by Keenan et al. 1992, the ratios between the intercombination and the forbidden components of the [C III] and [Si III] multiplets are similar within a broad range of electron temperatures (5000–20,000 K) and densities ( $10^2$ – $10^6$  cm<sup>-3</sup>). Therefore, if the forbidden component of the C III]<sub>1908</sub> multiplet was detected, the forbidden component of the Si III]<sub>1892</sub> multiplet should also be detected, which is not the case. Therefore, this identification is unlikely.

#### 4.1. Density of the SL Formation Region

The density of the line formation region is significantly different for the two kinematical components. The low-velocity component is not detected in C III]<sub>1908</sub>, providing a lower limit to  $R_2 = \text{Si III]}_{1892}/\text{C III]}_{1908} \geq 13$ . In a collisional plasma this indicates that the electron density of the gas is  $10^{10} \leq N_e \leq 10^{12}$  cm<sup>-3</sup> and the electron temperature is  $4.5 \leq \log T_e \leq 4.7$ . This very high density, as well as the velocity of the emission, strongly suggests that this component is produced in the stellar atmosphere.

The high-velocity component is detected both in Si III]<sub>1892</sub> and C III]<sub>1908</sub> and  $R_2 = 0.7$ . The low SNR of the C III]<sub>1908</sub> line makes this value for  $R_2$  very uncertain, and hence no constraints can be derived from Figure 4.

#### 4.2. Variability

The Si III]<sub>1892</sub> and C III]<sub>1908</sub> lines of RU Lup are highly variable, as shown by the flux variations among the 21 low-dispersion observations of RU Lup available in the *IUE* Final Archive. The Si III]<sub>1892</sub> and C III]<sub>1908</sub> variations are not correlated, and there are, in fact, two observations obtained on 1986 March 4 in which the Si III]<sub>1892</sub> line is detected, but not the C III]<sub>1908</sub> line. The absence of C III]<sub>1908</sub> emission corresponds to dates when the Si III]<sub>1892</sub> flux was high. No significant variations are detected in timescales of just few hours.

The line ratio  $R_2$ , is also variable and ranges between 1.2 and 3.7, but given the low dispersion of the spectra we cannot determine whether both or only one of the components is variable. Also the 1907 Å feature is contributing to the C III]<sub>1908</sub> fluxes.

The Si III]<sub>1892</sub> variability is correlated with the optical, while the C III]<sub>1908</sub> is not (see Fig. 8). The correlation between optical (*V*-band) and the Si III]<sub>1892</sub> flux points out that most of the Si III]<sub>1892</sub> emission is associated with the

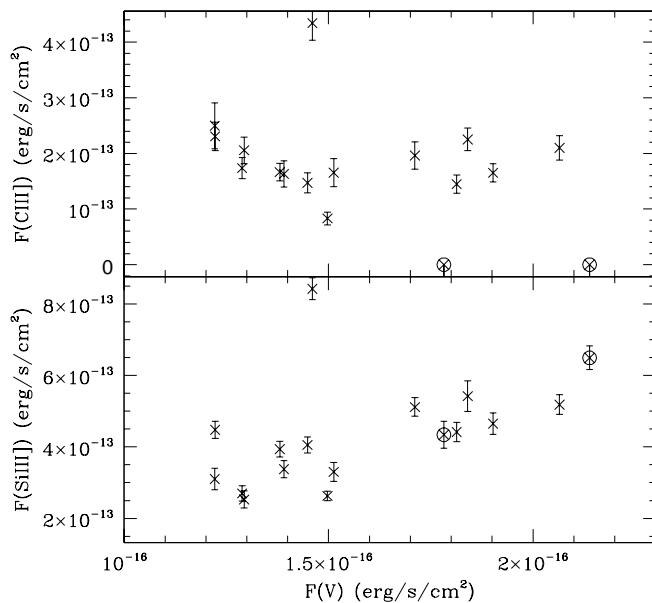


FIG. 8.—Variation of RU Lup SL fluxes with the optical flux derived from  $V$  magnitudes obtained with the *IUE* FES Camera. The observations were obtained with the *IUE*. The data marked with open circles correspond to nondetection of the  $C\text{ III}]_{1908}$  line.

star. This provides further confirmation on the stability of the low-velocity component associated with the star, which seems to be the dominant component during the *IUE* observations. On the other hand, the  $C\text{ III}]_{1908}$  flux has remained approximately constant apart from a flarelike episode in 1986 June 26, when both SL fluxes increased significantly without a stellar counterpart. This suggests that the  $C\text{ III}]_{1908}$  line is not emitted on the stellar surface.

#### 4.3. The Peculiar Feature in the RU Lup Spectrum at 1907 Å

This feature could be generated by blueshifted gas emitting in the  $C\text{ III}]_{1908}$  line. The inferred radial velocity is then,  $-260\text{ km s}^{-1}$ , which is close to the blue edge of the  $\text{Si III}]_{1892}$  line. This velocity corresponds also to the blue edge of the absorption component in the P-Cygni-like profile of the  $\text{Mg II}$  lines measured the same date with the *HST* + GHRS (see Fig. 9).

The  $\text{Mg II}$  profile of RU Lup consists of a very broad emission component that extends from radial velocity 0 to velocities as high as  $500\text{ km s}^{-1}$  and a broad blueshifted absorption component. The absorption component does not have an asymmetric black trough profile, as would be expected if the lines were formed in a spherical expanding envelope and produce standard P Cygni profiles. In fact, the absorption component is rather symmetric and saturates in the central core instead of in the blue edge. Moreover, the extent of the absorption component changes significantly from the *HST* to the *IUE* observations (the FWHM increases from  $\sim 180\text{ km s}^{-1}$  in the *HST* spectra to  $\sim 280\text{ km s}^{-1}$  in the *IUE* ones). The blue edge of the absorption component is at  $\sim -200\text{ km s}^{-1}$  in the  $\text{Mg II}$  *HST* observations. However, this blue edge moves to  $\sim -300\text{ km s}^{-1}$  in the *IUE* profiles surpassing the velocities at which the (presumably)  $C\text{ III}]_{1908}$  feature is detected (see Fig. 9). In consequence, the  $C\text{ III}]_{1908}$  feature could be well formed in the wind if, occasionally, it is heated up close to the terminal

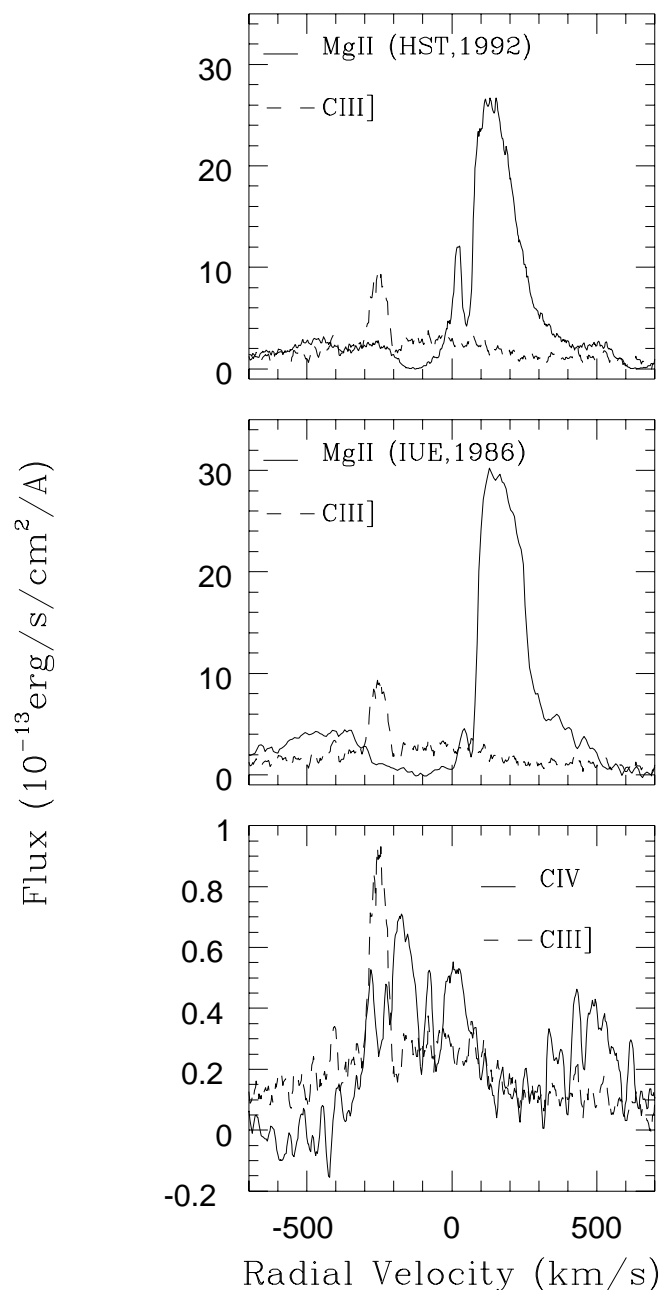


FIG. 9.— $C\text{ III}]_{1908}$  profile in 1992 (dashed line) is overplotted on the profiles of the  $\text{Mg II}$  (UV1) lines obtained in 1992 with the *HST* (top panel), on the  $\text{Mg II}$  (UV1) lines obtained in 1986 with the *IUE* (middle panel), and on the  $C\text{ IV}$  (UV1) profile obtained in 1992 with the *HST* (bottom panel).

speed. The nondetection of the  $\text{Si III}]_{1892}$  line suggests that the temperature of this plasma is higher than  $\log T_e \sim 4.6$  so the ionization fraction of the  $\text{Si III}]_{1892}$  goes below a 20% (see Fig. 4). The detection of a narrow feature in the  $C\text{ IV}$  line at the high-velocity edge of the  $C\text{ III}]_{1908}$  feature also suggests that the wind heats up as the velocity rises and shocks at the terminal velocity of a warm, dense wind.

The variations in the  $\text{Mg II}$  profile between the observations obtained with the *IUE* and *HST* would then indicate the existence of significant variations in the regime of the wind. We have not detected, however, significant differences between the spectra obtained with similar exposure times ( $\sim 90$  minutes) just two days apart in July, 1985 (LWP06367 and LWP06379) and between those and the



one obtained in 1986 (LWP07743), which is plotted in Fig. 9 (see GF for more information on these observations). Therefore, if there is any variation in the wind regime, it seems to occur in the rather large timescales. Unfortunately, there are not further UV observations of RU Lup which allow us to test simultaneous variations of these spectral tracers with time.

## 5. DISCUSSION

RY Tau and RU Lup are two classical T Tauri systems (star + disk) seen from very different orientations. The RY Tau system is seen close to edge-on; the star rotation velocity is very large,  $V \sin i = 51.6 \pm 4 \text{ km s}^{-1}$  (Hartmann & Stauffer 1989), eclipse-like minima are detected in the light curve (Grinin 1992), and the polarization is very high (Nadeau & Bastien 1986). The RU Lup system seems to be seen close to pole-on. The very small rotation period, which is not accompanied by the usual signs of high rotation velocity (e.g., high X-ray flux), as well as the low extinction (Hutchinson et al. 1989) are indications in this sense. Therefore, the joint analysis of the SL profiles of both systems allows to further constrain the wind geometry.

The broad SL profiles require a broad range of velocities in the line formation region. The profiles cannot be properly modeled without making a detailed physical model that includes assumptions on the wind drive and structure (density, velocity law, and equation of state). Fortunately, the SL lines are optically thin, and some further insight into the properties of the wind can be derived from naive geometrical models. We should use the simplest geometry: the spherical. Spherically symmetric surfaces can be used to model stellar winds, spherical “caps” can be used to model polar winds or bow shaped surfaces, and spherical segments can be used to model latitude-dependent winds. In Figures 10 and 11 we present the predicted wind profiles for two of these naive geometric models:

1. *Spherical stellar wind* (Fig. 10).—The SL line emission is assumed to be produced in a spherical expanding shell around the T Tauri star; the wind velocity vector is normal to the spherical surface and the velocity of the wind is assumed to be constant over the shell. The T Tauri star is surrounded by an accretion disk, which occults a hemisphere. The observed line profiles are represented as a function of the radius of the shell and the inclination of the disk ( $i$ ) such that  $i = 0^\circ$  represents a line of sight parallel to the disk axis and  $i = 90^\circ$  represents a disk seen edge-on. As shown in Figure 10, the stellar disk occults a fraction of the receding part of the shell which decreases as the shell radius increases. Therefore, the emission has to be produced in an extended envelope in order for the star not to occult the receding part of the outflow and produce a redshifted component to the profile. A lower limit to the shell radius of  $\geq 1.5 R_*$  is derived if the synthetic profiles are compared with those of RY Tau, the “edge-on” system. No constraint can be derived for the pole-on system since the receding part of the outflow is occulted by the disk and not by the star. Obviously, the profiles do not fit within this very naive model, as expected given the characteristics of the TTS winds.

2. *Spherical segments* (Fig. 11).—This geometry represents an optically thin emitting surface that is occulted neither by the star nor by the disk and which covers a fraction of the sphere (axially symmetric). As above, the

wind velocity vector is assumed to be normal to the surface and the velocity to be constant over it. The grid of models represented in Figure 11 corresponds to various inclinations ( $i = 0^\circ$  represents a line of sight parallel to the axis of the segment) and latitude ranges. As shown in the figure, belts close to the equator produce double-peaked profiles, the separation between the peaks being related with the inclination. On the other hand, spherical caps produce single-peaked profiles whose degree of broadening is related with the inclination. The models also point out the difficulties of producing extended red wings without giving rise to the formation of double-peaked profiles. This is feasible only if most of the emitting material is concentrated in the spherical cap smoothing down the double peaked structure. These results are roughly consistent with the inclinations of the RY Tau and RU Lup systems. Redshifted gas is detected in the SL profiles of RY Tau, which is the system seen close to edge on, especially in the  $\text{Si III}]_{1892}$  line. On the contrary, a strong, narrow, blueshifted component seems to have been detected in the  $\text{C III}]_{1908}$  profile of RU Lup, the system seen close to pole-on. In both cases, most of the emission seems to come from spherical caps or polar structures. In this sense, it is difficult to understand the coexistence of a broad and a narrow component in the SL profiles of RU Lup. It could be possible that the broad SL emission is partly tracing the velocity law in the acceleration region of the flow (also traced by the  $\text{Mg II}$  absorption). However, to get further insight, it is required to obtain high signal-to-noise ratio observations where the  $\text{C III}]_{1908}$  profile can be properly analyzed and compared with the  $\text{Si III}]_{1892}$  and the  $\text{Mg II}$  (UV1) lines.

In summary, the region traced by the SL lines emission is most likely bow-shaped and aligned with the disk axis. The location of this structure can be constrained for only RY Tau, and a lower limit to the distance between the star and the SL formation region of  $1.5 R_*$  is derived from the detection of redshifted gas in the SL profiles; this limit is also consistent with the derived from the SL variability (see § 3.2). Further constraints on the location and size of the shocked region can be derived if some assumptions are made on the shock mechanism.

### 5.1. Constraints to Wind Models

The observational information about how the TTS outflow is initiated is contained within 14 AU around the source, in a “black box” (see Eisloefel et al. 2000) that is not accessible to direct imaging even for stars as close as RU Lup or RY Tau, which are just 140 pc away from the Sun. The generation of shock waves at such small scales is not a trivial problem. For stars like RY Tau or RU Lup, which are not deeply embedded in the parent molecular cloud, the shock waves cannot be interpreted as the result of the interaction of the TTS wind with the environment. Hence, shock waves have to be built into the wind dynamics becoming a useful tool to discriminate between wind models.

In the last years, much work has been devoted to the analysis of shock wave formation in disk winds. Gómez de Castro & Pudritz (1993, hereafter GdCP) pointed out that shock waves could be easily generated in centrifugally driven MHD disk winds. In this model, the shock is produced if the magnetic tension from the toroidal component is so strong as to recollimate (pinch) the flow back to the

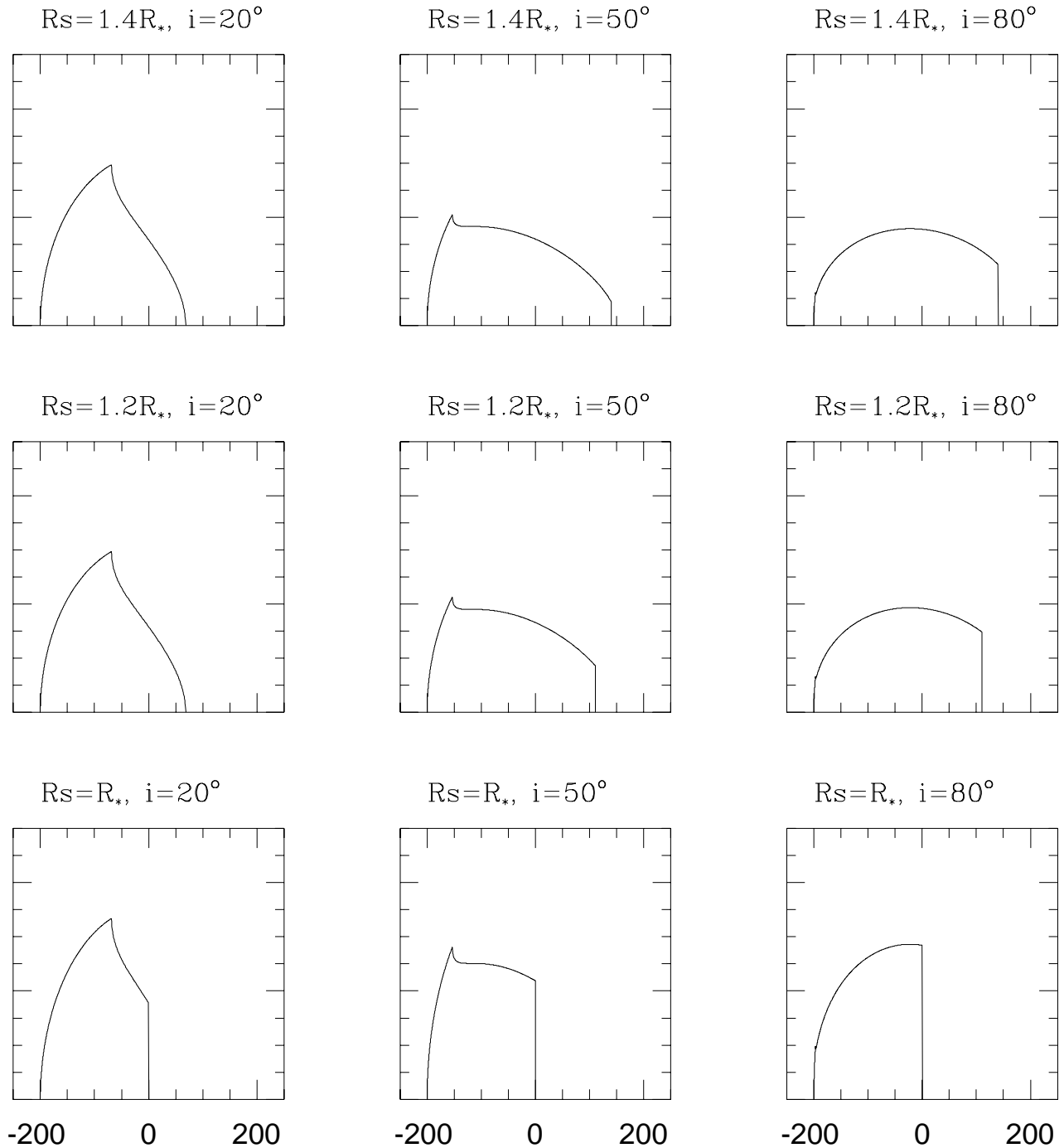


FIG. 10.—Models of optically thin line profiles produced in a spherical expanding shell; the wind velocity vector is normal to the spherical surface and the velocity of the wind is assumed to be constant over the shell. The profiles are represented in velocity space ( $\text{km s}^{-1}$ ) as a function of the radius of the shell and the inclination of the disk ( $i$ ) such that  $i = 0^\circ$  represents a line of sight parallel to the disk axis and  $i = 90^\circ$  represents a disk seen edge-on.

axis at super-Alfvénic speeds. In this sense, the magnetic field acts as a nozzle that efficiently collimates and accelerates the outflow. This physics applies to all kind of centrifugally driven MHD winds independently of the source of the wind (star, disk, magnetosphere; see e.g. Pelletier & Pudritz 1993 [hereafter PP]; Contopoulos & Lovelace 1994; Vlahakis & Tsinganos 1998).

The SL lines could be formed either in the warm post-shock gas generated in MHD oblique shocks or in the photoionized precursor of strong shocks ( $V \sim 200 \text{ km s}^{-1}$ ). In fact, the GdCP model has been already successfully applied

to reproduce the profiles of the optical forbidden lines. In general, the characteristics of the shocked region depend on the model used, but whenever a wind solution giving rise to the formation of large-scale jets is sought, they are similar in the asymptotic limit to those described by GdCP. A major source of uncertainty is the poor knowledge of the thermal properties of the gas at the base of the wind and the degree of efficiency of the wind that controls the terminal velocity of the gas. An additional source of uncertainty is the obliquity of the shock since the fraction of kinetic energy released into the heat channel in comparison with that

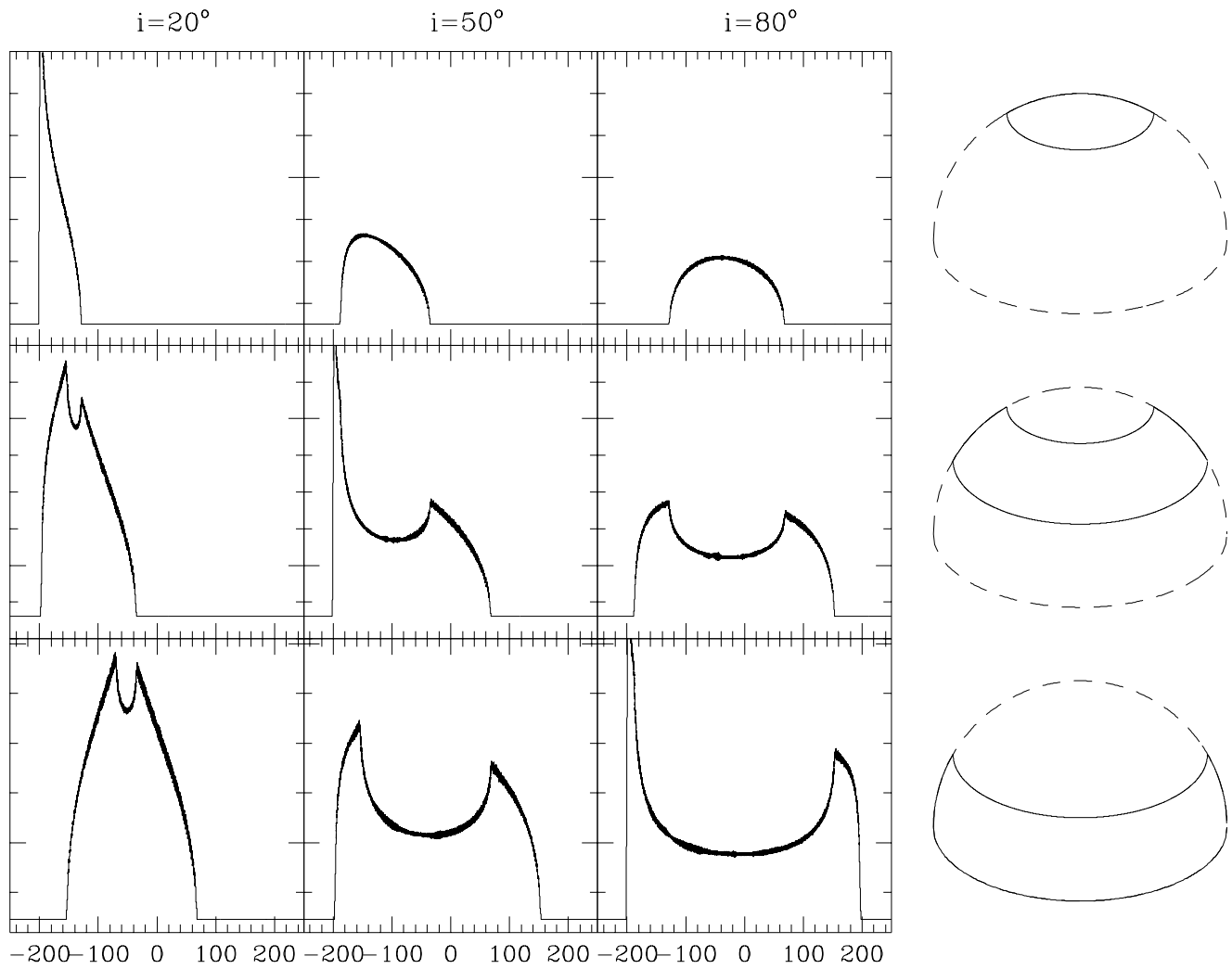


FIG. 11.—Models of optically thin line profiles produced in segments of a spherical expanding shell to show up the dependence with latitude; the wind velocity vector is normal to the surface of the expanding segments and the velocity of the wind is assumed to be constant over them. The profiles are represented in velocity space ( $\text{km s}^{-1}$ ) as a function of the radius of the latitude of the segment and the inclination of the disk ( $i$ ) (as in Fig. 10,  $i = 0^\circ$  represents a line of sight parallel to the disk axis).

released in the magnetic channel depends on the obliquity and on the plasma  $\beta$  (Ericson & Bazer 1960; see also Ouyed & Pudritz 1993 for a detailed application to PP models).

In summary, there is a broad range of thermal properties (for the shock wave) that can be accommodated within the available theoretical models. Hence, no significant constraints to wind/jet models can be derived from them. This is not so for other parameters of the shock wave such as density, location and characteristic size. For instance, although disk winds are very often used to explain the generation of jets and the optical forbidden line emission region in young stars, the solutions explored in the literature generate low-density winds that pinch at large distances (at least several tens of AUs) from the star.

#### 5.1.1. Constraints from the Density of the Shock Wave

The determination of the density of the shock wave hangs on the assumptions made for the treatment of the emitting plasma. Within the context of centrifugally driven MHD winds, the SL lines could be formed either in the warm postshock gas in oblique or mild shocks or in the photoionized precursor of strong shocks ( $V \sim 200 \text{ km s}^{-1}$ ). In the first case, as shown in § 3.1, the SL emission is produced in a

collisionally dominated plasma and the density derived is  $3 \times 10^9 \leq N_e \leq 10^{11} \text{ cm}^{-3}$ . Notice that if the plasma is highly nonthermal, a recalculation of the ionization equilibrium equations would be required with new collisional cross sections taking into account the departure of the electrons from a Maxwellian distribution in the magnetized plasma. However, recent determination of magnetic fields in TTSs jets point out that the field is close to equipartition.

Let us now assume that the SL emission is produced in the photoionized precursor of a strong shock. In this case, the observed radial velocity of the gas would correspond to the preshock velocity. In this limit the kinetic energy would be released into heating and the shock could be treated as hydrodynamical. A classical example are the shock models calculated for the formation of bow shocks (see, e.g., Hartigan et al. 1987). These models predict the formation of the  $\text{C III}]_{1908}$  and  $\text{Si III}]_{1892}$  lines observed in the high excitation Herbig-Haro objects. In these objects  $R_2 \sim 0.3$  (see Gómez de Castro & Robles 1999 for a complete compilation of the *IUE* data), which is significantly smaller than the values derived for the TTSs in this work. Also, the density of the SL-emitting gas in Herbig-Haro objects is  $\sim 10^2\text{--}10^3 \text{ cm}^{-3}$ , while the density of the SL-emitting gas in

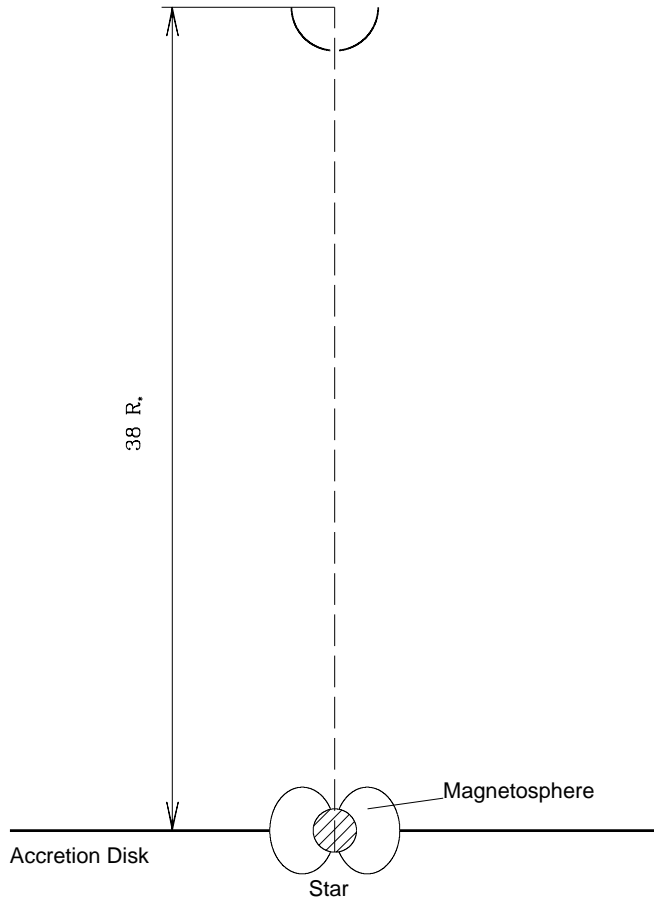


FIG. 12.—Sketch representing the location and characteristic dimensions of the SL-emitting region in RY Tau. The distance between the shocked region and the star can be significantly smaller than plotted since only an upper limit can be derived from the current data (see text). This plot is based on the assumption that the density of the SL emitting region is  $\sim 10^{10} \text{ cm}^{-3}$ . In a lower density plasma with  $N_e \sim 10^8 \text{ cm}^{-3}$  both the radius of the emitting region and the upper limit to the distance between the star and the shock would increase by a factor of 10.

RY Tau is  $\geq 10^5 \text{ cm}^{-3}$ . No shock models have been developed for higher densities, and there are only some predictions available for very high densities ( $10^{10.5} - 10^{13} \text{ cm}^{-3}$ ) (see Appendix). These models suggest that the density of the emitting gas is very high ( $\sim 10^{10.5} \text{ cm}^{-3}$ ), in agreement with the value derived above.

Disk winds cannot produce such a high-density shock waves. Therefore, if high-resolution spectra confirm that the  $1665 \text{ \AA}$  feature detected in the RY Tau spectrum is produced in the wind by emission from the  $\text{O III}]_{1665}$  doublet ( $\lambda\lambda 1660.8, 1666.2$ ), it should be concluded that winds originate from the star or its magnetosphere.

### 5.1.2. Constraints from the Location and Size of the Shock Wave

Some constraints on the location and size of the shock wave can be derived from the continuity equation (mass-loss rate conservation). In the following we should assume that the flow traced by the optical  $[\text{O I}]_{6300}$  line (Hartigan et al. 1995) is the same than the traced by the UV semi-forbidden lines. Also, a fiducial density of  $\sim 10^{10} \text{ cm}^{-3}$  will be assumed for the UV line formation region.

If the emission is assumed to arise in a collimated beam, the mass-loss rate can be derived from the UV lines as

$$\dot{M}_w = \mu m_H N V S,$$

or

$$\dot{M}_w = 9.8 \times 10^{-10} M_\odot \text{ yr}^{-1} \left( \frac{N}{10^{10} \text{ cm}^{-3}} \right) \times \left( \frac{V}{200 \text{ km s}^{-1}} \right) \left( \frac{R}{R_*} \right)^2,$$

where  $\mu$  is the mean molecular weight of the wind material,  $m_H$  is the mass of a hydrogen atom,  $N$  and  $V$  are the density and velocity of the wind,  $S$  is the cross section of the flow, and  $R$  is its characteristics radius. This mass-loss rate is expected to be similar to that derived from the  $[\text{O I}]_{6300}$  measurements, which is  $3.1 \times 10^{-9} M_\odot \text{ yr}^{-1}$  (we have allowed for a correction by a factor of 2 with respect to the estimate of  $\dot{M}_w$  derived by Hartigan et al. [1995] because the length of the line emission region is  $0.7$  according to Hirth et al. 1997), so

$$\left( \frac{N}{10^{10} \text{ cm}^{-3}} \right) \left( \frac{V}{200 \text{ kms}^{-1}} \right) \left( \frac{R}{R_*} \right)^2 = 3.16,$$

or

$$\frac{R}{R_*} = 1.78 \left( \frac{N}{10^{10} \text{ cm}^{-3}} \right)^{-1/2} \left( \frac{V}{200 \text{ kms}^{-1}} \right)^{-1/2},$$

and, therefore, the radius of the SL-emitting layer is expected to be of the order of the stellar radius. This value could be underestimated since the mass-loss rate derived from the  $[\text{O I}]_{6300}$  line is most probably a lower limit to the true mass-loss rate. Both the high density of the SL formation region and the fact that the  $[\text{O I}]_{6300}$  profile is much narrower than the SL profiles suggest that much of the wind passes through shocks at densities above the  $[\text{O I}]_{6300}$  critical density. However, as  $R$  depends on the square root of  $\dot{M}_w$ , the radius estimated is not expected to change by more than a factor of  $\sim 3$  ( $\dot{M}_w \simeq 10^{-8} M_\odot \text{ yr}^{-1}$ ).

Moreover, as the conservation of mass requires that  $NVR^2 = \text{constant}$ , if the velocity of the outflow is the same in the high-density region, where the UV SL emission is produced, as in the lower density region, where the  $[\text{O I}]_{6300}$  line is observed, we derive

$$\frac{N_{\text{UV}}}{N_{[\text{O I}]}} = \left( \frac{R_{[\text{O I}]}}{R_{\text{UV}}} \right)^2.$$

A drop in density by 4 orders of magnitude between the high and low-density regions implies an increase in the jet radius by 2 orders of magnitude, namely, if  $R_{\text{UV}} \simeq 2 R_*$  then  $R_{[\text{O I}]} = 200 R_* \simeq 2.2 \text{ AU}$ . As the centroid of RY Tau  $[\text{O I}]_{6300}$  emission is located within  $0.3$  (or  $42 \text{ AU}$ ) of the star (Hirth et al. 1997), this indicates that the opening angle of the outflow is  $\geq 6^\circ$ , which is consistent with the typical opening angles derived for T Tauri stars close to the source (see Eisloffel et al. 2000 for a recent review).

If we assume that the opening angle of the flow,  $\theta$ , keeps constant between the star and the region where the  $[\text{O I}]_{6300}$  line is emitted, then

$$\theta = 2 \times \arctan \left( \frac{R_{\text{UV}}}{d_{\text{UV}}} \right),$$

and therefore a distance of  $\leq 38 R_*$  (or  $0.43 \text{ AU}$ ) is derived between the SL emission region and the star. This tiny distance corresponds to a spatial scale of milliarcseconds, which is within the “black box” that cannot be resolved unless interferometric techniques are used. A sketch of this

TABLE 4  
LINE FLUX

OBJECT	C III] <sub>1908</sub>			Si III] <sub>1892</sub>		
	$F_o^a$	$F_d^b$	$\log (L/L_\odot)$	$F_o^a$	$F_d^b$	$\log (L/L_\odot)$
RY Tau .....	3.4	1.28	-4.105	3.2	1.23	-4.12
RU Lup .....	15.0	34.4	-2.68	Low/High <sup>c</sup> 21.0 / 7.6	Low/High 46.4 / 16.8	Low/High -2.55 / -2.99

<sup>a</sup> Observed flux in the line in units of  $10^{-14}$  ergs  $\text{cm}^{-2}$   $\text{s}^{-1}$ .

<sup>b</sup> Dereddened flux in the line in units of  $10^{-13}$  ergs  $\text{cm}^{-2}$   $\text{s}^{-1}$ .

<sup>c</sup> See text for details of the two components.

region summarizing the results of this work for RY Tau is shown in Figure 12. If this small size and radius would be confirmed, we should conclude that the disk cannot be the source of the wind. Again, this determination relies on the value of the density and henceforth, on the O III]<sub>1665</sub> doublet.

Finally, we would like to mention that the variability of the SL lines can be readily explained within the context of centrifugally driven MHD winds. Slight variations in the lever arm can move significantly the location of the shocked region along the axis of symmetry. In this case, the SL flux variations could be tracing the motion of the shocked region along the axis and the timescale of these variations could be tracking the motion of the shock wave. If the shock wave is assumed to move at a velocity,  $V_w$ , similar to the wind velocity, then the shock wave should travel a distance,  $d_w$ , such that

$$d_w \leq 1.3 \times 10^{12} (\text{cm}) \frac{V_w}{200 \text{ kms}^{-1}} = 18.6 R_\odot \frac{V_w}{200 \text{ kms}^{-1}},$$

where we have used a fiducial value of  $200 \text{ km s}^{-1}$  for  $V_w$ . Notice that  $d_w \simeq 7.4 R_*$  is consistent with a distance  $\leq 38 R_*$  between the shock wave and the star.

## 6. CONCLUSIONS

In summary, we have analyzed the high-resolution profiles of the C III]<sub>1908</sub> and Si III]<sub>1892</sub> semiforbidden UV lines as well as their variability for two TTSs: RY Tau and RU Lup. The major properties of these lines are summarized in Table 4. We have found the following:

1. The SL observed in RY Tau cannot be produced on the stellar surface, so they are not associated with accretion shocks. The line emission is produced in the wind.

2. The SL emission from RU Lup is produced partly in the stellar atmosphere and partly in the wind. The dominant component to the Si III]<sub>1892</sub> line is stellar and could be associated with a chromospherically active region close to the stellar pole.

3. The luminosity of the UV SL ( $L = 10^{-4} L_\odot$ ) of RY Tau is comparable to that of the optical [O I]<sub>6300</sub> line, which is the often used to parameterize the wind luminosity in T Tauri stars.

4. The wind profiles of the UV SL are significantly broader than those of the optical forbidden lines. This broad UV profile cannot be produced in a narrow collimated beam. The most likely source is emission from a bow-shaped shock wave formed at the base of the optical jet.

5. A puzzling narrow feature is observed close to the C III]<sub>1908</sub> line. The feature is blueshifted by  $-260 \text{ km s}^{-1}$ ,

which corresponds to the wind terminal velocity measured in the P Cygni profile of the Mg II (UV1) lines. These data are suggestive of the existence of a dense, warm wind within few stellar radii, which ends in a high-velocity shock. The detection of a narrow feature in the C IV line at the high-velocity edge of the C III]<sub>1908</sub> feature is also suggestive in this sense. Further observations are instrumental to confirm this interpretation.

6. The SL lines trace a high density and temperature component of the base of the optical jets. We have derived density and temperature constraints to the emitting gas for RY Tau. A lower limit to the gas density of  $N_e > 10^5 \text{ cm}^{-3}$  is derived. It follows from the assumption that the SL are produced in a collisional plasma that  $4.7 \leq \log T_e \leq 5.0$ . Moreover, a density constraint can be derived ( $10^9 \text{ cm}^{-3} \leq N_e \leq 10^{11} \text{ cm}^{-3}$ ) provided that the 1665 Å feature observed in the low-dispersion IUE spectra of RY Tau is produced by O III]<sub>1665</sub> emission in the wind. High-resolution spectra in this range are required to confirm this density determination.

7. Provided that the shock wave traced by the UV SL and that traced by the [O I]<sub>6300</sub> are produced in the same outflow, constraints have been derived on the location and size of the SL emitting region for RY Tau. From the continuity equation we derive a radius of the shocked surface of  $1.78 R_*$  and an upper limit to the distance to the star of  $38 R_*$ .

8. The UV semiforbidden lines have an enormous potential to the study of the physics of outflow in T Tauri stars since the density of the shock at the base of the jet is extremely sensitive to the models, especially when disk versus stellar winds are analyzed.

Finally, we would like to stress the relevance of high-resolution spectroscopic data for the proper usage of the C III]<sub>1908</sub> and Si III]<sub>1892</sub> lines in the analysis of the TTSs atmospheres and circumstellar environment. As shown in this work, there can be a significant contribution either from the wind (or jet) and the atmosphere to the line flux. They also can be formed in accretion shocks.

We thank Constantino Ferro Fontán, Sergei Lamzin, Valentín Bujarrabal, Benjamin Montesinos, and Reinhart Mundt for stimulating discussions and Ilana Dashevsky from the Spectrographs Group (STScI) for her assistance in the interpretation of the GHRS data. We are indebted to the VILSPA staff for their assistance during the development of the project. We thank an anonymous referee for his comments. This research was supported by the MEC through grant PB97-267.

## APPENDIX

## ESTIMATE OF THE SIZE OF THE SL-EMITTING REGION MAKING USE OF HIGH-DENSITY SHOCKS MODELS

In these models the shock wave has been considered as plane parallel (i.e., one-dimensional) and stationary in Eulerian coordinates. The lines fluxes have been computed for a broad range of infall velocities [ $200 \leq V_0(\text{km s}^{-1}) \leq 400$ ] and gas densities [ $10.5 \leq \log N_0(\text{cm}^{-3}) \leq 13$ ]. The  $\text{C III}]_{1908}$  and  $\text{Si III}]_{1892}$  lines are found to be formed via *electron collisional excitation* before the shock front. Since the SL lines are formed before the shock front and they are optically thin, the emissivities calculated for the stellar case are fully applicable to any shock wave, provided that the internal extinction within the shock front is negligible. If not, the detailed geometry of the shock front and its orientation with respect to the observer should be considered. Therefore, following Gómez de Castro & Lamzin (1999), the observed flux  $F$  at the Earth can be expressed as

$$F = \frac{I^n S_{\text{sw}}}{d^2} \exp(-0.92A_\lambda),$$

where  $I^n$  ( $\text{ergs s}^{-1} \text{cm}^{-2} \text{st}^{-1}$ ) is the intensity of an optically thin line in the direction perpendicular to the shock front,  $S_{\text{sw}}$  is the surface of the whole shock wave;  $d$  is the distance to the star, and  $A_\lambda$  is the interstellar extinction at wavelength  $\lambda$ . The  $I^n$  values are plotted for the  $\text{Si III}]_{1892}$  line and a grid of models in Figure 1 of Gómez de Castro & Lamzin (1999; hereafter GdCL). Making use of low-dispersion *IUE* observations, GdCL, derive the following shock parameters for RY Tau:  $10.5 < \log N_e < 11$  and  $200 \text{ km s}^{-1} < V < 250 \text{ km s}^{-1}$  (see Fig. 3 in GdCL). We have selected for this calculation the shock model corresponding to  $V = 200 \text{ km s}^{-1}$  and  $\log N = 10.5 \text{ cm}^{-3}$ . The model predicts that the intensity of the  $\text{Si III}]_{1892}$  line is  $I^n = 7.73 \times 10^4 \text{ ergs s}^{-1} \text{cm}^{-2} \text{st}^{-1}$ . The extinction towards RY Tau is  $A_V = 0.55 \text{ mag}$  and hence, assuming the extinction towards the star is well described by the standard interstellar medium extinction law,  $A_{\lambda 1892} = 1.42 \text{ mag}$  and

$$S_{\text{sw}} = 15.3 \times 10^{24} \text{ cm}^2 = 0.07 \text{ AU}^2.$$

Therefore a characteristic radius of  $1.6 \times 10^{12} \text{ cm}$  (or  $9.2 R_*$ ) is derived for the emitting region; an hemispheric surface is assumed. The true radius of the emitting region depends on the distance to the star and the morphology of the shock wave. The thickness of the emitting layer can be derived from the shock calculations, and it is  $7 \times 10^{10} \text{ cm}$ ; therefore, the total emitting volume is  $1.1 \times 10^{36} \text{ cm}^3$ . This emitting volume corresponds to a sphere with radius  $3.8 R_*$ .

## REFERENCES

- Arnaud, M., & Rothenflug, R. 1985, *A&AS*, 60, 425  
Brown, A., Ferraz, M. C. de M., & Jordan, C. 1984, *MNRAS*, 207, 831  
Contopoulos, J., & Lovelace, R. V. E. 1994, *ApJ*, 429, 139  
Edwards, S., Cabrit, S., Strom, S. E., Heyer, I., Strom, K. M., & Anderson, E. 1987, *ApJ*, 321, 473  
Eisloffel, J., Mundt, R., & Ray, T. P., & Rodriguez, L. F. 2000, *Protostars and Planets IV*, ed. V. Manning & A. Boss (San Diego: Academic)  
Ericson, W. B., & Bazer, J. 1960, *Phys. Fluids*, 3, 631  
Fireman, G. F., & Imhoff, C. L. 1989, *NASA IUE Newsl.*, 40, 10  
Gómez de Castro, A. I. 2001, in *ASP Conf. Ser. 223*, 11th Cambridge Workshop on Cool Stars, Stellar Systems, and the Sun, ed. R. J. García-López, R. Rebolo, & M. R. Zapatero-Osorio (San Francisco: ASP), 29  
Gómez de Castro, A. I., & Franqueira, M. 1997, *ULDA Access Guide to T Tauri Stars Observed with IUE* (ESA-SP 1205; Noordwijk: ESA)  
Gómez de Castro, A. I., & Lamzin, S. A. 1999, *MNRAS*, 304, L41  
Gómez de Castro, A. I., & Pudritz, R. E. 1993, *ApJ*, 400, 748  
Gómez de Castro, A. I., & Robles A. 1999, *INES Access Guide to Herbig-Haro objects Observed with IUE* (ESA-SP 1237; Noordwijk: ESA)  
González-Riestra, R., Cassatella, A., Solano, E., Altamore, A., & Wamsteker, W. 2000, *A&AS*, 141, 343  
Grinin, V. P. 1992, *Astron. Astrophys. Trans.*, 3, 17  
Haman, F. 1994, *ApJS*, 93, 485  
Hartigan, P., Edwards, S., & Ghandour, L. 1995, *ApJ*, 452, 736  
Hartigan, P., Raymond, J., & Hartmann, L. 1987, *ApJ*, 316, 323  
Hartmann, L., & Stauffer, J. R. 1989, *AJ*, 97, 873  
Hirth, G. H., Mundt, R., & Solf, J. 1997, *A&AS*, 126, 437  
Holm, A., & Rice, G. 1981, *NASA IUE Newsl.*, 15, 74  
Hutchinson, M. G., Evans, A., Davies, J. K., & Bode, M. F. 1989, *MNRAS*, 237, 683  
Jordan, C. 1969, *MNRAS*, 142, 501  
Jordan, C., Ferraz, M. C. de M., & Brown, A. 1982, *Proc. 3d IUE Conf.*, Madrid, (Noordwijk: ESA), 83  
Keenan, F. P., Dufton, P. L., & Kingston, A. E. 1987, *MNRAS*, 225, 859  
Keenan, F. P., Feibelman, W. A., & Berrington, K. A. 1992, *ApJ*, 389, 443  
Koenigl, A., & Pudritz, R. E. 2000, *Protostars and Planets IV*, 2000, ed. V. Manning & A. Boss (San Diego: Academic)  
Lamzin, S. A. 1998, *Astron. Rep.*, 42, 322  
Lamzin, S. A. 2000, *Astron. Lett.*, 26, 589  
Lindler, D. J. 1993, *Proc. HST Calibration Workshop*, 27  
Nadeau, R., & Bastien, P. 1986, *ApJ*, 307, 5  
Ouyed, R., & Pudritz, R. E. 1993, *ApJ*, 419, 255  
Pelletier, G., & Pudritz, R. E. 1992, *ApJ*, 394, 117  
Pérez, M. R. 1991, *ESA IUE Newsl.*, 38, 27  
Rodríguez, P. M., González-Riestra, R., Schartel, N., & Wamsteker, W. 1999, *A&AS*, 139, 183  
Shu, F., Najita, J. R., Shang, H., & Li, Z.-Y. 2000, *Protostars and Planets IV*, ed. V. Manning & A. Boss (San Diego: Academic)  
Stickland, D. J. 1980, *ESA IUE Newsl.*, 5, 30  
Vlahakis, N., & Tsinganos, K. 1998, *MNRAS*, 298, 777